Simulation of Indentation Fracture in Crystalline Materials Using Mesoscale Self-Assembly

Venkat R. Thalladi,[†] Alexander Schwartz,[†] Jennifer N. Phend,[†]
John W. Hutchinson,[‡] and George M. Whitesides*,[†]

*Contribution from the Department of Chemistry and Chemical Biology, and
Division of Engineering and Applied Sciences, Harvard University, 12 Oxford Street,
Cambridge, Massachusetts 02138*

Received April 22, 2002

Abstract: A new physical model based on mesoscale self-assembly is developed to simulate indentation fracture in crystalline materials. Millimeter-scale hexagonal objects exhibiting atom-like potential functions were designed and allowed to self-assemble into two-dimensional (2D) aggregates at the interface between water and perfluorodecalin. Indentation experiments were performed on these aggregates, and the stresses and strains involved in these processes were evaluated. The stress field in the aggregates was analyzed theoretically using the 2D elastic Hertz solution. Comparison of the experimental results with theoretical analysis revealed that fracture develops in regions subjected to high shear stress *and* some, albeit low, tensile stress. The potential for the broader application of the model is illustrated using indentation of assemblies with point defects and adatoms introduced at predetermined locations, and using a two-phase aggregate simulating a compliant film on a stiff substrate.

Introduction

Indentation is a technique widely used to probe processes important in materials: fracture, defect nucleation, adhesion, friction, wear.[1−5] Indentation is difficult to study experimentally at the scale of atoms; instead, computer simulations and physical models of indentation are often used.[6−9] The most elementary physical models of indentation use bubble rafts.[10,11] Bubbles are experimentally convenient models for atoms,[12] but they have limitations: they are inherently spherical, and the interactions between them are nondirectional and difficult to tailor in strength and character. Here we report a new physical model for materials based on self-assembled arrays of millimeter-scale objects floating at a fluid−fluid interface,[13] and we describe the use of

this system to simulate indentation fracture in crystalline materials. This model is, in effect, an extension of bubble rafts. The objects used in this model can be made in a variety of shapes and sizes (micrometers to millimeters);[14,15] the direction, strength, and sign of the interactions between them are under the control of the investigator;[16] they form ordered two-dimensional (2D) assemblies.[17,18]

We have demonstrated previously that millimeter-scale solid objects suspended at the water/perfluorodecalin (PFD) interface and interacting by capillarity self-assemble into ordered 2D aggregates.[18] Here we suggest that these aggregates can, with appropriate design of the components, serve as 2D models for crystals and other solids and can simulate fracture behavior under indentation. Most of our prior work has been carried out using *solid* polymer plates.[18] The potential function describing the interactions between these plates is not a realistic model of an atomic potential: it consists of a smoothly descending attraction (due to capillarity) and a steeply ascending (hard) contact repulsion (Figure 1a).[16] In this work, we have used soft hexagonal objects (Figure 1b) designed to have pairwise potential function that shows a softer repulsion, and thus to better simulate a Morse potential (or, with appropriate design, some other potential). These objects support large positive menisci at the water/PFD interface for capillary attraction and exhibit

* Corresponding author. E-mail: gwhitesides@gmwgroup.harvard.edu.
† Department of Chemistry and Chemical Biology.
‡ Division of Engineering and Applied Sciences.

(1) Lawn, B. *Fracture of Brittle Solids*; Cambridge University Press: Cambridge, 1993.
(2) Gane, N.; Pfaelzer, P. F.; Tabor, D. *Proc. R. Soc. London* **1974**, *A340*, 495−517.
(3) Kelchner, C. L.; Plimpton, S. J.; Hamilton, J. C. *Phys. Rev.* **1998**, *B58*, 11085−11088.
(4) Johnson, K. L. *Contact Mechanics*; Cambridge University Press: Cambridge, 1985.
(5) Rabinowicz, E. *Friction and Wear of Materials*; McGraw-Hill: New York, 1965.
(6) Landman, U.; Luedtke, W. D.; Burnham, N. A.; Colton, R. J. *Science* **1990**, *248*, 454−461.
(7) Meakin, P. *Science* **1991**, *252*, 226−234.
(8) Lynden-Bell, R. M. *Science* **1994**, *263*, 1704−1705.
(9) Bulatov, V.; Abraham, F. F.; Kubin, L.; Devincre, B.; Yip, S. *Nature* **1998**, *391*, 669−672.
(10) Georges, G. M.; Meille, G.; Loubet, J. L.; Tolen, A. M. *Nature* **1986**, *320*, 342−344.
(11) Gouldstone, A.; Van Vliet, K. J.; Suresh, S. *Nature* **2001**, *411*, 656.
(12) Bragg, L.; Nye, J. F. *Proc. R. Soc. London* **1947**, *A190*, 474−481.
(13) Bowden, N.; Terfort, A.; Carbeck, J.; Whitesides, G. M. *Science* **1997**, *276*, 233−235.

(14) Choi, I. S.; Bowden, N. B.; Whitesides, G. M. *Angew. Chem., Intl. Ed.* **1999**, *38*, 3078−3081.
(15) Clark, T. D.; Tien, J.; Duffy, D. C.; Paul, K. E.; Whitesides, G. M. *J. Am. Chem. Soc.* **2001**, *123*, 7677−7682.
(16) Grzybowski, B. A.; Bowden, N.; Arias, F.; Yang, H.; Whitesides, G. M. *J. Phys. Chem. B* **2001**, *105*, 404−412.
(17) Bowden, N.; Choi, I. S.; Grzybowski, B.; Whitesides, G. M. *J. Am. Chem. Soc.* **1999**, *121*, 5373−5391.
(18) Bowden, N. B.; Weck, M.; Choi, I. S.; Whitesides, G. M. *Acc. Chem. Res.* **2001**, *34*, 231−238.
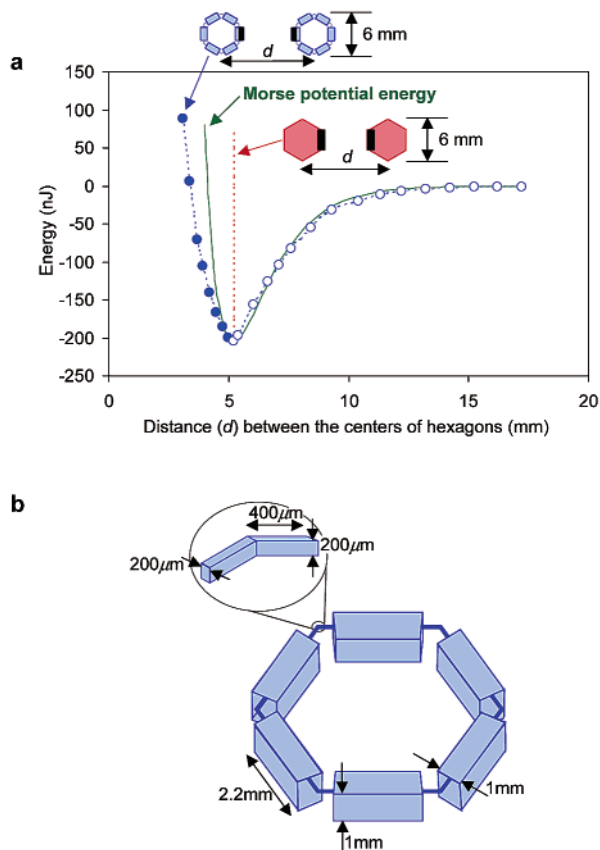
Figure 1. (a) Comparison of potential functions for the interactions between solid (red) and soft (blue) hexagonal objects floating at the interface of water and PFD. The dimensions of interacting side faces of both solid and soft hexagons are 2.2 mm long and 1 mm high. The attractive parts (○) of the potential curves were obtained by finite element methods,[16] and the repulsive parts (●) were obtained from experimental force measurements. Physical contact of noncompressible, solid hexagons leads to steep repulsion. The linkers built within the soft hexagons make them compressible and result in smooth repulsion. Bold lines indicate the sides of the hexagons that are patterned hydrophobic. A Morse potential energy curve, derived from the equation $E = [E_D(1 - e^{k(d-d_{min})^2}] - E_D$, is drawn (green line) for comparison. The values of E_D (dissociation energy, 204 nJ) and d_{min} (5.2 mm, distance corresponding to minimum energy) are obtained from the experiment. The value of constant k is set to 0.65 to fit the curve to the experimental results. The constant k is proportional to the square root of the anharmonicity constant. (b) Hexagonal object designed to have a soft repulsive potential. Six rectangular blocks are attached in a hexagonal geometry by thin linkers (see inset). It is possible to control the attractive and repulsive parts of the potential function because it is possible to tailor the area of the exposed faces of the blocks and the density of the polymer relative to the fluid phases (to control the attractive capillary forces) and the stiffness of the linkers (to control the elastic repulsive forces). The hexagons are placed at the water/PFD interface in the orientation shown here.

smooth compression for elastic repulsion. These hexagonal objects were fabricated in poly(dimethylsiloxane) (PDMS) using a mold prepared by rapid prototyping[19] and two-level photolithography.[20] The similarity between the experimental and Morse potential functions is shown in Figure 1a.[21] The directionality of the interactions is determined by the pattern of hydrophobicity and hydrophilicity of the edge faces.

(19) Qin, D.; Xia, Y.; Whitesides, G. M. *Adv. Mater.* **1996**, *8*, 917–919.
(20) Choi, I.; Weck, M.; Jeon, N. L.; Whitesides, G. M. *J. Am. Chem. Soc.* **2000**, *122*, 11997–11998.
(21) Atkins, P. W.; Friedman, R. S. *Molecular Quantum Mechanics*; Oxford University Press: New York, 1997; p 337.
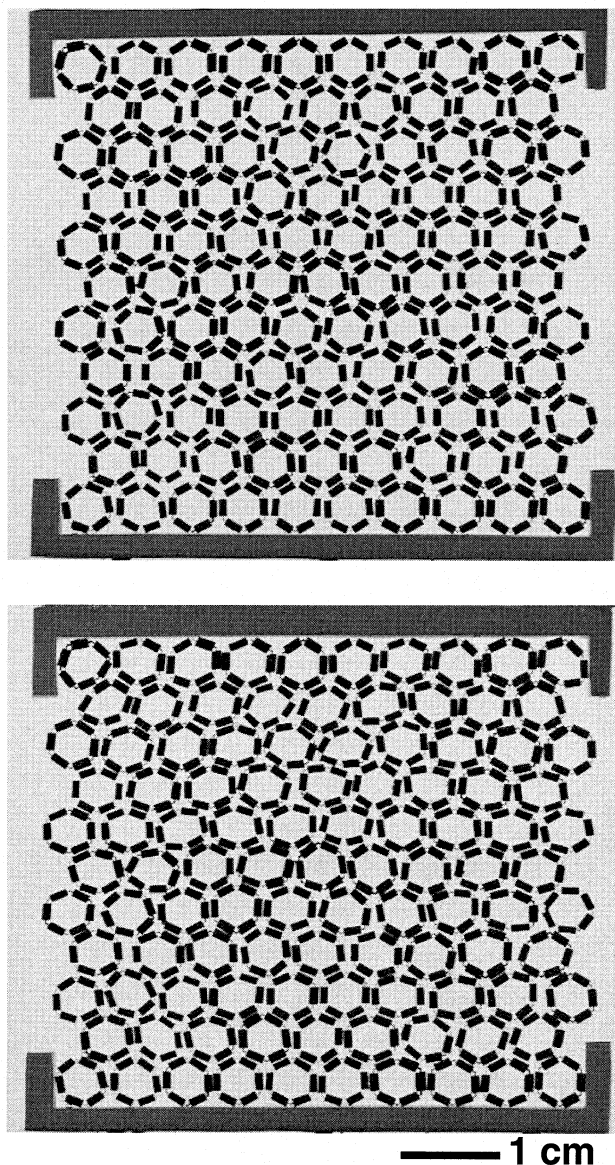
Figure 2. Compression of a 2D assembly of hexagons. The hexagons were placed at the water/PFD interface and assembled between two frames of PDMS. The lower frame is attached to a stationary metal plate, and the upper frame (in the figure) was pushed toward the lower at a constant speed of 8×10^{-3} m s^{-1}. Measurements of stress and strain at various stages of the compression were used to calculate Poisson's ratio and Young's modulus of the system. The image on the top shows the assembly before compression, and the one on the bottom shows the assembly during compression.

Results and Discussion

Our objective in this work is to model indentation. Because we are working with a new system, we first explored two parameters that strongly determine many of the mechanical properties of a solid body: Poisson's ratio (ν) and Young's modulus (E). We performed compression experiments on an assembly of ∼100 hexagons (Figure 2) and measured ν and E of the system. The experimental values of ν (∼0.35) and E (∼4 × 10^4 N m^{-2}) demonstrate the compressibility of hexagons and the resemblance of these aggregates to real materials: these moduli are representative of certain gels and biological tissues (e.g., $E_{Physarum \text{ cytoplasmic strands}}$ ≈ 2 × 10^4 N m^{-2});[22] typical values for stiffer materials are ∼4 × 10^8 (polyethylene) and ∼2 × 10^{11} N m^{-2} (stainless steel). We utilize the values of ν and E
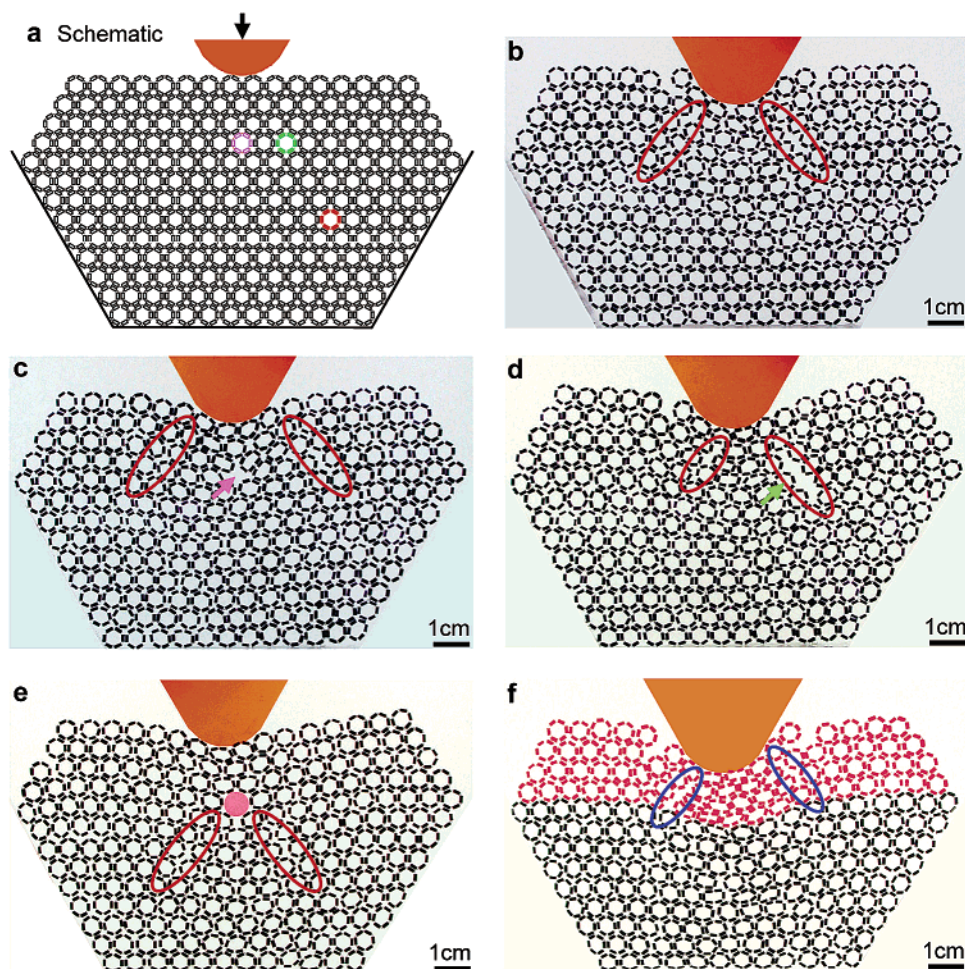
Figure 3. (a) Schematic view of the aggregates subjected to indentation. The indenter was positioned symmetrically on the surface of the aggregate and loaded in the direction indicated by the arrow. Point defects were introduced in separate experiments at positions indicated by pink (c), green (d), and red hexagons (no experimental figure shown). An adatom was introduced at the position indicated by the pink hexagon (e). The shape of the aggregate conforms to the geometry of the frame (shown in black) in which it was constructed. (b−f) Experimental images of indentation fracture in self-assembled aggregates: (b) Hertzian-type cone cracks develop in a defect-free aggregate under indentation. (c) Indentation of an aggregate similar to that shown in (b), but with a point defect (indicated by arrow) on the loading axis. Fracture planes are displaced outward in a symmetrical fashion relative to those shown in (b). (d) Indentation of an aggregate similar to that shown in (b), but with a point defect (indicated by arrow) off the loading axis. Unlike fractures in (c), fracture planes are displaced asymmetrically. (e) Indentation of an aggregate containing a noncompressible adatom. Fracture develops deeper in the aggregate than in (b) or (c). (f) Indentation of an aggregate with a phase boundary. The top four rows (those nearer to the tip) are more compressible than the rest of the aggregate. The fracture developed in the compressible phase does not propagate beyond the phase boundary. In all images, for simplicity, the frame around the aggregate is not shown.

obtained in the compression of the self-assembled raft in evaluating the shear stress and strain required for indentation fracture in the following experiments.

Figure 3a shows the experimental design of the indentation experiments. The hexagons were hydrophobic on all six lateral sides, and capillary interactions between these edges cause them to self-assemble into hexagonal close-packed structures. We constructed self-assembled aggregates of ∼200 hexagons within a frame whose geometry was compatible with the hexagonal symmetry of the aggregate. Experimentally, different aggregates could be constructed easily with ∼200 components; working with larger numbers of components was difficult.[23] As will be shown later, these aggregates are sufficiently large that their boundaries do not influence the results obtained. We used an

indenter whose surface was also hydrophobic. The hexagons were attracted to the tip of the indenter at the contact point; qualitatively similar behavior occurs with atoms in many real indentation experiments.[6] Indentation loads were applied to the aggregates by controlled displacement of the indenter using an electric motor. We used a loading speed of 8×10^{-3} m s^{-1} in all the experiments. Speeds higher than this value resulted in out-of-plane buckling of the hexagons. The results of the experiments were qualitatively similar for slower speeds (∼5 $\times 10^{-3}$ m s^{-1}). The force acting on the aggregate was monitored during the entire experiment.

We indented different types of aggregates. Three features were common to all indentations: (1) The fracture patterns in all the cases were analogous to Hertzian cone cracks.[24] (2) The deformation of the aggregate was reversible for low loads, as in real systems.[1] (3) The results of these experiments were qualitatively similar and reproducible (over at least five repeats).

(22) Davidson, L. A.; Oster, G. F.; Keller, R. E.; Koehl, M. A. R. *Dev. Biol.* **1999**, *209*, 221−238.

(23) Our attempts to work with larger assemblies with 500−1000 components have not been successful: these assemblies were fractured or developed defects because of the shear and vibration generated in the water/PFD system during the process of self-assembly.

(24) Frank. F. C.; Lawn, B. R. *Proc. R. Soc. London* **1967**, *A299*, 291−306.
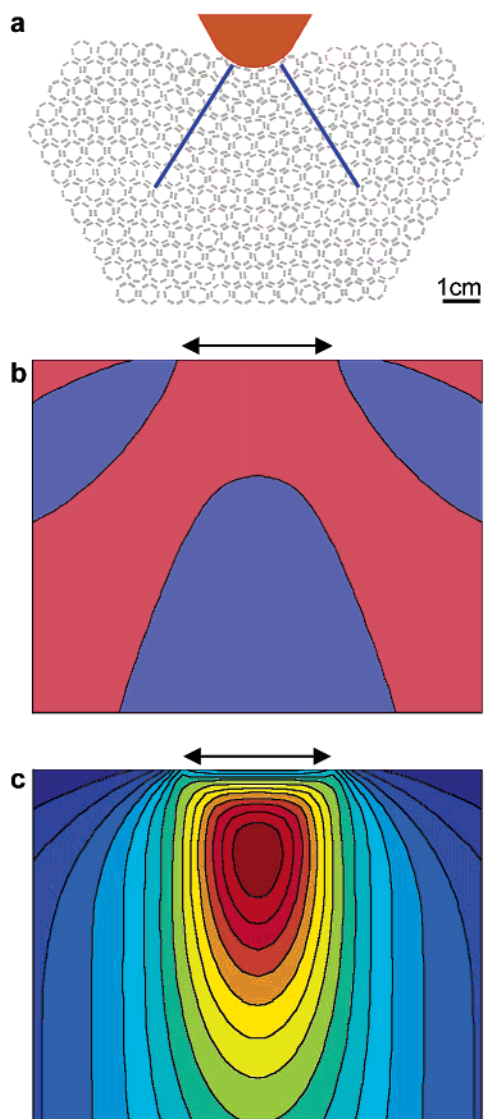
Figure 4. (a) Experimental image of a defect-free aggregate under indentation stress. The frame around the aggregate is not shown for clarity. The deformation of hexagons is large closer to the indenter tip and the loading axis and decreases gradually with increasing distance from the tip and loading axis. Blue lines indicate potential fracture planes. (b) Theoretical contour plot of maximum in-plane principal stress. The double-headed arrow indicates the contact width of the indenter. Red and purple regions indicate compressive and tensile components of the maximum principal stress. Quantitatively, the tensile stress is a very small fraction ($\sim$5%) of the average stress ($\bar{\sigma}$) imposed by the indenter. (c) Theoretical contour plot of maximum in-plane shear stress. The double-headed arrow indicates the contact width of the indenter. The largest shear stress ($\sim\bar{\sigma}/2$) occurs directly beneath the indenter tip (red regions); it diminishes gradually to the levels of $\sim\bar{\sigma}/10$ in the outer blue regions.

We begin with the description of the indentation of a defect-free aggregate. Figure 4a is a snapshot of a defect-free aggregate under indentation stress prior to the development of fracture; it shows the extent to which deformation is concentrated near the indenter tip. Using the 2D elastic Hertz solution[25] for the indentation of an isotropic solid, we have plotted the stress field distribution in Figure 4b,c. The indenter used in this solution is similar to the one used in our experiments: it is rigid and possesses a circular tip. The maximum in-plane principal stress

(25) Muskhelishvili, N. I. *Some Basic Problems of the Mathematical Theory of Elasticity*; Noordhoff: Groningen, 1953.

is predominantly compressive (red regions in Figure 4b) and occurs throughout the lattice; its tensile component (blue regions in Figure 4c) is a small fraction ($\sim$5%) of the average stress ($\bar{\sigma}$) applied by the indenter. This small fraction of tensile stress acts on planes roughly parallel to the blue lines indicated in Figure 4a. The maximum in-plane shear stress attains almost $\bar{\sigma}/2$ in regions below the indenter tip and acts on planes inclined at roughly 45° to the vertical. These stresses have been determined from a continuum theory of the lattice and therefore represent averages over multiple components. We note that stresses between components immediately under the indenter tip may not be accurately described by the Hertz solution. The solution should, however, provide an accurate description of the stresses between components away from the immediate vicinity (couple of atomic spacings) of the tip.

Upon further loading, fracture occurs below the surface (Figure 3b). Fracture appears to align with planes subjected to high shear stress and some, albeit low, tensile stress. Planes experiencing even higher shear stresses exist directly beneath the indenter, but these planes are also subjected to significant normal compressive stresses that act to suppress the fracture. The measured indenter force at the onset of fracture in the defect-free aggregate is $\sim$11.2 $\times$ 10^{-4} N. Based on the elastic Hertz solution and the measured modulus, this implies local critical shear stress (τ_c) $\sim$25 N m^{-2} and shear strain (γ_c) $\sim$2 $\times$ 10^{-3} at the point of fracture initiation. Figure 3b shows that the hexagons close to the outer boundary experience very little deformation; this observation suggests that the outer boundary conditions do not significantly influence the initiation of cracking, as would also be expected from elastic stress analysis.

We introduced defects by selectively removing hexagons from pre-assembled aggregates or by adding adatoms with higher compressive stiffness. We studied three cases for point defects (Figure 3a): the defect was positioned (a) on the loading axis close to the tip, (b) along a potential fracture plane close to the tip, and (c) along a potential fracture plane far away from the tip. The distant defect (c) had no effect on indentation fracture. In cases a and b, stress redistribution by point defects led to changes in the stress field of the aggregate. As a result, the fracture occurred along different planes (Figure 3c,d). A symmetrically located defect resulted in the symmetric displacement of fracture planes (compare parts b and c of Figure 3) and an unsymmetrically located defect resulted in an unsymmetrical displacement of fracture planes (compare parts b and d of Figure 3). The force required for the crack initiation in both cases a and b is lower than that required for crack initiation in the defect-free aggregate (22% and 28% lower in symmetrically and unsymmetrically located defects, respectively).

Two further examples suggest that this method has the potential to be broadly applicable in the study of fracture and indentation. Figure 3e shows indentation of an aggregate with an adatom introduced in the same place where the point defect in case a is located. We used a solid (noncompressible) circular adatom that is slightly larger than the surrounding hexagons. Surprisingly, unlike indentation in a lattice containing point defects (Figure 3c,d), the cracks appeared deeper in the aggregate (Figure 3e). The force required for the crack initiation ($\sim$9.2 $\times$ 10^{-4} N) in this aggregate with a solid adatom is slightly more than that required in the related aggregate with a point defect (case a; $\sim$8.6 $\times$ 10^{-4} N).
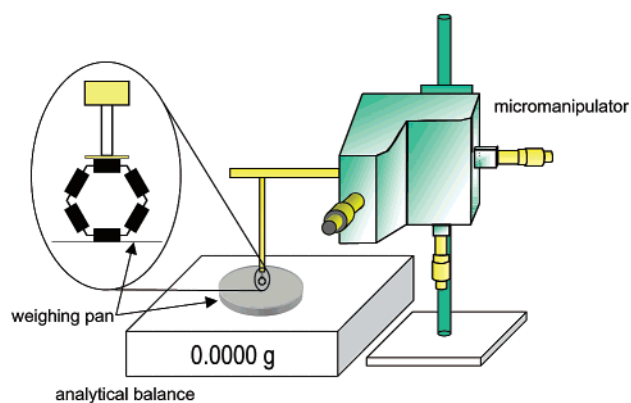
Figure 3f illustrates the indentation of a two-phase aggregate. The top four rows of the aggregate are made of hexagons (100 μm $\times$ 200 μm linkers) that are softer than the rest of the hexagons (200 μm $\times$ 200 μm linkers). Upon loading, the deformation is largely confined to the more compressible phase nearer to the tip. The fracture is arrested at the boundary of the stiffer phase. The force required for the crack initiation ($\sim$4 $\times$ 10^{-4} N) in this aggregate is very low, as expected. The ability to construct multiphase systems with tailored mechanical properties is an additional tool that can be used in understanding and designing damage-resistant thin films and graded materials.[26]

This model system needs to be improved in three ways to provide more accurate simulation of indentation and fracture. (1) It should be made three-dimensional. (2) It should incorporate larger numbers of objects. (We can work with large numbers ($>$1000) of objects only with effort until the fabrication methods are improved.[27]) (3) The radius of curvature of the indenter tip should be increased. (In the current system, the tip is unphysically small: the radius of curvature of the tip would be 1.2 nm if each hexagon were considered an atom of diameter 3 Å.) It remains to be seen whether the phenomena observed in the present work are scalable to large numbers of particles and larger indenters.

Conclusion

Millimeter-scale objects with engineered shapes and potential functions offer a new approach to the simulation of properties of materials. The components used in our model can be made in different shapes (isotropic or anisotropic) and sizes (micrometer to millimeter) and can mimic organic crystalline materials. It is possible to introduce grain boundaries, adatoms, and point defects into assemblies at predetermined locations. Crack initiation and propagation can be monitored optically and continuously. We believe that our method can be extended to other physical processes (e.g., friction and the nucleation and propagation of dislocations under other stresses, including tension and shear). The potential functions describing interactions between objects interacting by capillarity can be readily obtained by finite element analysis;[16] embedding these potential functions in multiparticle simulations of these processes should provide an instructive comparison of the ability of the computer methods to predict the properties of materials reliably, in a model system in which all the experimental parameters are well-defined and under the control of the experimenter. Gouldstone, Van Vliet, and Suresh have shown that 2D bubble rafts can be used to model the unusually high local stress required for defect nucleation in nanoindented, face-centered cubic crystals.[11] The 2D model of crystals based on mesoscale self-assembly is an improvement on bubble raft models in terms of adjustable interaction potentials and directionalities, shapes, and sizes of the objects. Application of these physical models to a wide range of materials, however, would optimally use 3D assemblies with larger numbers of objects. Further work in the development of

(26) Suresh, S. *Science* **2001**, *292*, 2447−2451.
(27) Our recent work (ref 15) shows that we can fabricate components having lateral dimensions as small as 10 μm, and we can form 3D self-assembled aggregates containing more than 100 000 components. Extending current work to smaller components and 3D aggregates, however, requires new methods for the fabrication of smaller components that exhibit atom-like potential functions and new means of monitoring indentation.

Scheme 1. Experimental Setup for Measuring the Potential Function

physical models for the simulation of properties of materials should thus focus on 3D systems containing at least 10 000 constituents.
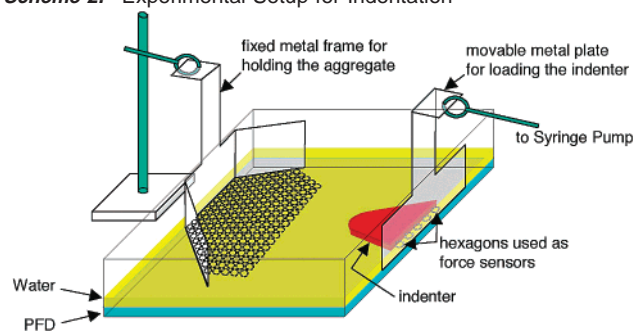
Experimental Section

Fabrication of Soft Hexagons. Masters with elevated hexagonal features of irradiated SU-8 photoresist (MicroChem, Newton, MA) were fabricated in two stages using photolithography. In each stage, a layer of resist was spun onto a silicon wafer, exposed to UV light through a photo mask, and developed in a solution of 1-methoxy-2-propanol acetate (Aldrich). The linkers were fabricated in the first stage and the blocks in the second; the blocks were aligned on the linkers using a mask aligner. The masters were silanized using a vapor treatment with (tridecafluoro-1,1,2,2-tetrahydrooctyl)-1-methyldichlorosilane ($C_8F_{13}H_4$-$SiCH_3Cl_2$, abbreviated as R-Si, United Chemical Technologies, Bristol, PA) for 2 h to prevent adhesion to PDMS.[19] Negative replicas of these masters were made in PDMS by curing a prepolymer (Sylgard 184, Dow-Corning) for 3 h at 65 °C against the silanized master. These PDMS masters were oxidized in a Harrick PDC-23G plasma cleaner and silanized with R-Si. Hexagons were fabricated by molding using the silanized PDMS masters: the molds were filled with PDMS prepolymer, excess polymer was removed by pressing the PDMS master between two glass slides, and the prepolymer was cured for 3 h at 65 °C. The hexagons were released from the PDMS masters by immersing the masters in ethanol for 2 h; they were dyed blue or red by soaking (for 3 h) in 1 M methylene chloride solutions of crystal violet or Sudan red.

Measurement of Potential Function. The attractive parts of the potential curves were obtained by finite element methods described previously;[16] the repulsive parts were obtained from the following experiment (Scheme 1). A hexagon was attached on one of its sides to a thin plate (6 $\times$ 2 $\times$ 0.5 mm^3) connected to a micromanipulator. The manipulator with the attached hexagon was placed next to an analytical balance (with a readability of 0.1 mg) such that the opposite side of the hexagon was positioned on the weighing pan. The hexagon was compressed between the weighing pan and the thin plate incrementally by screwing the manipulator in 200-μm steps. At each step, the force exerted by the hexagon was calculated by reading the weight on the balance. High-resolution digital images were taken at each step, and the extent of compression of the hexagon was extracted from these images for each step. The energy required for the compression of the hexagon was calculated at each step; the values of energy were normalized to match the values obtained from finite element analysis and used in drawing the potential energy curve shown in Figure 1a.

Construction and Indentation of the Aggregates. Deionized water and PFD (Aldrich) were taken in a polypropylene tray into which a metal frame of the shape shown in Figure 3a was immersed and clamped (Scheme 2). Dyed hexagons were placed at the water/PFD

Scheme 2. Experimental Setup for Indentation

interface, and a row of hexagons was arranged close to the frame. Additional rows of hexagons were allowed to self-assemble by moving the hexagons closer to the first row; the remaining hexagons were removed from the interface once an aggregate of the desired size was constructed. An indenter (in the shape shown in Figure 3) was carved from a 1.5 mm thick sheet of PDMS and placed at the water/PFD interface. A metal plate (connected to a syringe pump) was inserted into the tray, and the indenter was positioned next to it. The indenter was loaded into the aggregate using the syringe pump/metal plate at a controlled speed, and the fracture patterns that developed in the aggregate were imaged. Five separate soft hexagons were attached at the rear side of the indenter; these hexagons acted as force sensors during the indentation. The force constant of these hexagons was determined from the experiment shown in Scheme 1. The extent of compression of these sensor hexagons was extracted from the digital images and used to calculate the force acting on the aggregate.